International Journal of Greenhouse Gas Control 129 (2023) 103966

Contents lists available at ScienceDirect

International Journal of Greenhouse Gas Control

journal homepage: www.elsevier.com/locate/ijggc

Assessing the impact of dip angle on carbon storage in saline reservoirs to aid site selection

Catherine Callas *, Anthony R. Kovscek, Sally M. Benson

Department of Energy Resources Engineering, Stanford University, Stanford, CA 94305, USA

ARTICLE INFO

Keywords:
CO_2 storage
Plume footprint
Secondary trapping
Dipping reservoirs

ABSTRACT

Reservoir dip angle and permeability significantly impact CO_2 plume migration and the amount of secondary phase trapping in storage formations. There is a fundamental trade-off between up-dip plume migration and secondary trapping that can be advantageous, or disadvantageous, for selecting an optimal CO_2 storage site. For example, low permeability reservoirs have limited plume migration up-dip, consequently, residual and solubility trapping are also limited. On the contrary, for highly permeable reservoirs, up-dip migration can be fast and extensive, leading to accelerated residual and solubility trapping. By performing a systematic simulation study of plume migration and secondary trapping in reservoirs with a range of permeabilities and dip angles, we found that having a dip angle of at least 1° and permeability of at least 500mD results in up to 88% of the plume being immobilized 100 years post-injection. In reservoirs with a permeability of at least 500mD, we can optimize the amount of immobilized CO_2 while limiting the amount of plume migration. As reservoir dip angles increase up to 2° and permeability increases, CO_2 plume migration increases progressively, and up to 8x more mass of CO_2 can migrate up-dip versus down-dip. At the same time, CO_2 solubility in brine and residual trapping work to decrease the plume volume and can immobilize 28% to 90% of the CO_2 plume over 100 years post-injection. Five influential parameters were identified that strongly influence the plume volume during the post-injection period for these dipping reservoirs: CO_2 saturation, residual gas saturation, CO_2 solubility in brine, CO_2 density, and formation permeability. We also investigated the impact of simulation grid resolution, the maximum non-wetting phase saturation, and the pore-size distribution parameter on predicted plume behavior. This work provides simple, reliable relationships between key site screening metrics, reservoir dip angle, and permeability to inform the site selection process and monitoring, measurement, and verification (MMV) design.

1. Introduction

Carbon capture and sequestration (CCS) will play a significant role in mitigating carbon emissions and that role is expected to grow over time (UNFCCC, 2017). CCS involves the injection of supercritical carbon dioxide (CO_2) into geological formations for long-term storage. A key element to the success of CCS is finding a suitable sequestration site that can store emissions securely over geological timescales. Understanding how the CO_2 plume will migrate in the reservoir over time is essential to the site selection and regulatory processes. An estimate of the plume footprint is used to identify pore space ownership issues and any potential leakage pathways through well infrastructures, faults, or fractures in the area (Frailey, 2013; NETL, 2017a; Wen and Benson, 2019). Secondary trapping, such as residual or solubility trapping, stabilizes or prevents plume migration, if significant (NETL, 2017a). During the site selection process, secondary trapping mechanisms should be identified and assessed (NETL, 2017b). In addition, the ability to predict the plume migration both spatially and temporally helps optimize the monitoring process (Doughty, 2010). To select an optimal storage site, the reservoir properties that influence plume migration and secondary trapping need to be considered. The reservoir dip angle is a reservoir property that significantly impacts plume migration and secondary trapping.

Saline reservoirs used for storage are often dipping, and dip significantly influences the storage process, including residual and solubility trapping, up-dip migration, and plume stabilization (Doughty and Pruess, 2004; M.A. Hesse, 2008; Kumar et al., 2004). Dip angles can range from 0° to gently dipping reservoirs in mid-Norway to 7° in the Vedder Formation in California to much higher values (Chadwick et al., 2004; Doughty, 2010). Many of these sloping regional saline reservoirs do not have structural closure, which could result in leakage from up-dip

* Corresponding author.
E-mail address: haycat@stanford.edu (C. Callas).

https://doi.org/10.1016/j.ijggc.2023.103966
Received 1 December 2022; Received in revised form 21 July 2023; Accepted 22 August 2023
Available online 7 September 2023

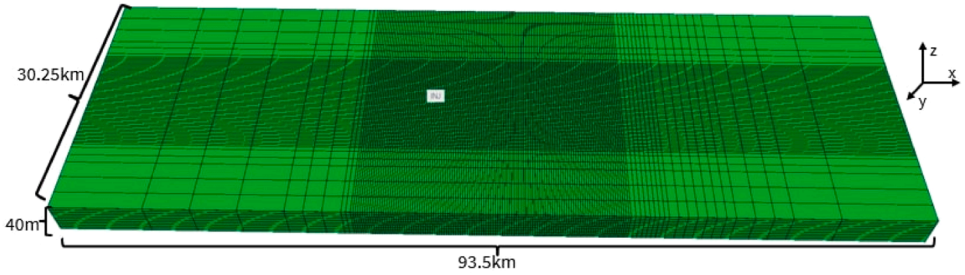

Fig. 1. Model Grid. The model is 40 m thick, with uniform grid blocks of 4 m in the z-direction. The reservoir extends 93.5 km in the x-direction and 30.25 km in the y-direction. The grid is refined around the injection well as detailed in Table 1.

Table 1
Description of the grid used for systematically comparing the influence of dip angle and permeability on plume migration and secondary trapping.

Vertical (Z-direction)			X-direction		Y-direction	
Permeability	Number of Grid Cells	Cell Size (m)	Number of Grid Cells	Cell Size (m)	Number of Grid Cells	Cell Size (m)
10-100 mD	10	4	1	10000	3	2000
500mD and 1D	20	2	3	5000	2	1000
			3	2000	1	500
			2	500	53	250
			118	250	1	500
			8	500	2	1000
			7	1000	3	2000
			3	2000		
			1	5000		
			1	10000		
Total Thickness: 40m			X-direction extent: 93,500m		Y-direction extent: 32,250m	

migration (Chadwick et al., 2008; M.A. Hesse et al., 2008). To assess this risk, the speed and distance of the CO_2 plume front and duration at which CO_2 remains mobile or positively buoyant needs to be estimated (Hesse et al., 2006). As CO_2 migrates up-dip due to buoyancy, capillary forces on the trailing edge of the plume trap CO_2 in the pore space, while at the leading edge, CO_2 dissolves in under-saturated brine (Doughty, 2010; Hesse et al., 2006).

In high permeability reservoirs, the CO_2 can migrate up-dip long distances (Kumar et al., 2004). At the same time, solubility and residual trapping increase as a larger volume of brine and rock interact with the mobile CO_2, that increases the storage security over time as they immobilize the CO_2 plume (IPCC, 2005; Kumar et al., 2004). Studies have shown that residual trapping will be the dominant trapping mechanism in sloping aquifers and is optimized in sloping reservoirs with small mobility ratios and high residual CO_2 saturation (Hesse et al., 2006, M.A. 2008). Increasing the slope of the aquifer leads to faster residual trapping as the CO_2 plume migrates up-dip faster and slumps more slowly (Hesse et al., 2006). Therefore, the reservoir dip angle strongly influences plume migration and the immobilization of the CO_2 plume.

Not only does the dip angle of a reservoir affect storage security, but aquifer permeability and formation dip were also shown to be the key parameters impacting the sweep efficiency (Gammer et al., 2011). Permeability and dip angle are critical determinants of sweep efficiency because they control the speed of CO_2 migration and pressure buildup (Goater et al., 2013).

Previous studies have utilized numerical modeling to examine the impact of dip angle in a particular location with a unique heterogeneity (Doughty, 2010; Doughty and Pruess, 2004; Wang et al., 2017). Additionally, analytical solutions have been developed in sloping confined aquifers and in unconfined reservoirs (Gupta and Bryant, 2010; Hesse et al., 2006, M.A. 2008; Juanes et al., 2010; Juanes and MacMinn, 2008; Vella and Huppert, 2006). Many of these studies do not include secondary trapping mechanisms in their analytical solutions or only include residual trapping. In addition, many of these solutions are one-dimensional or two-dimensional and can be challenging to apply with the information available during the site screening process.

During a multi-stage site screening process, such as the one outlined in (Callas et al., 2022), the ability to estimate the impact that the reservoir dip angle and permeability have on plume migration and secondary trapping helps differentiate potential storage sites. During the site ranking stage, homogeneous reservoir characteristics are used because this is generally the information available early in the screening process (e.g., before a detailed site characterization is performed). Currently, there is no way to estimate the impact between reservoir characteristics available at the site screening and ranking phase on plume migration and secondary trapping without numerical simulation.

To address these issues, we systematically investigated the influence of the reservoir dip angle and permeability on the CO_2 plume footprint and secondary trapping mechanisms in homogeneous reservoirs. We also investigated the impact of grid resolution, the maximum non-wetting saturation, and the pore size distribution parameter in constitutive relations for multiphase flow. This work aims to provide simple, reliable relationships between key site screening metrics, reservoir dip angle, and permeability to inform the site selection process.

2. Methods

For these studies, we focus on homogeneous, gently dipping reservoirs. A 3-D cartesian grid is used with refined cells in the area where the plume is located near the injection well. Grid cells have a uniform thickness of 4 m for permeabilities of 10 mD, 50 mD, and 100 mD. Permeabilities of 500 mD and 1000 mD required finer grid cells in the z-direction of 2 m. The reservoir extends 93.5 km in the x-direction and 30.25 km in the y-direction to simulate an infinitely acting reservoir (Fig. 1). These dimensions were chosen to ensure that there was no pressure interference between the pressure front and constant pressure boundaries and that the CO_2 plume migration remained within the reservoir model. The center of the grid near the injection well uses 250 m grid cell blocks in the x- and y-directions for the area that the plume extends. The grid block size gets progressively larger in the x- and y-directions (Table 1). The thickness of the reservoir is 40 m. In Appendix A, we present a grid sensitivity study to justify the grid dimensions selected.

2.1. Model setup

The simulations were carried out using Computer Modeling Group (CMG) GEM (Computer Modeling Group, 2019). The system is simplified to be a water-CO_2 reservoir with a temperature 65 °C at a depth of 2000 m. The water table starts from 10 m below the ground surface, and reservoir pressure is hydrostatic with reference to the water table. We assume a continuous supercritical CO_2 injection with a constant rate of 1 million metric tonnes per year for 20 years and monitor for 100 years

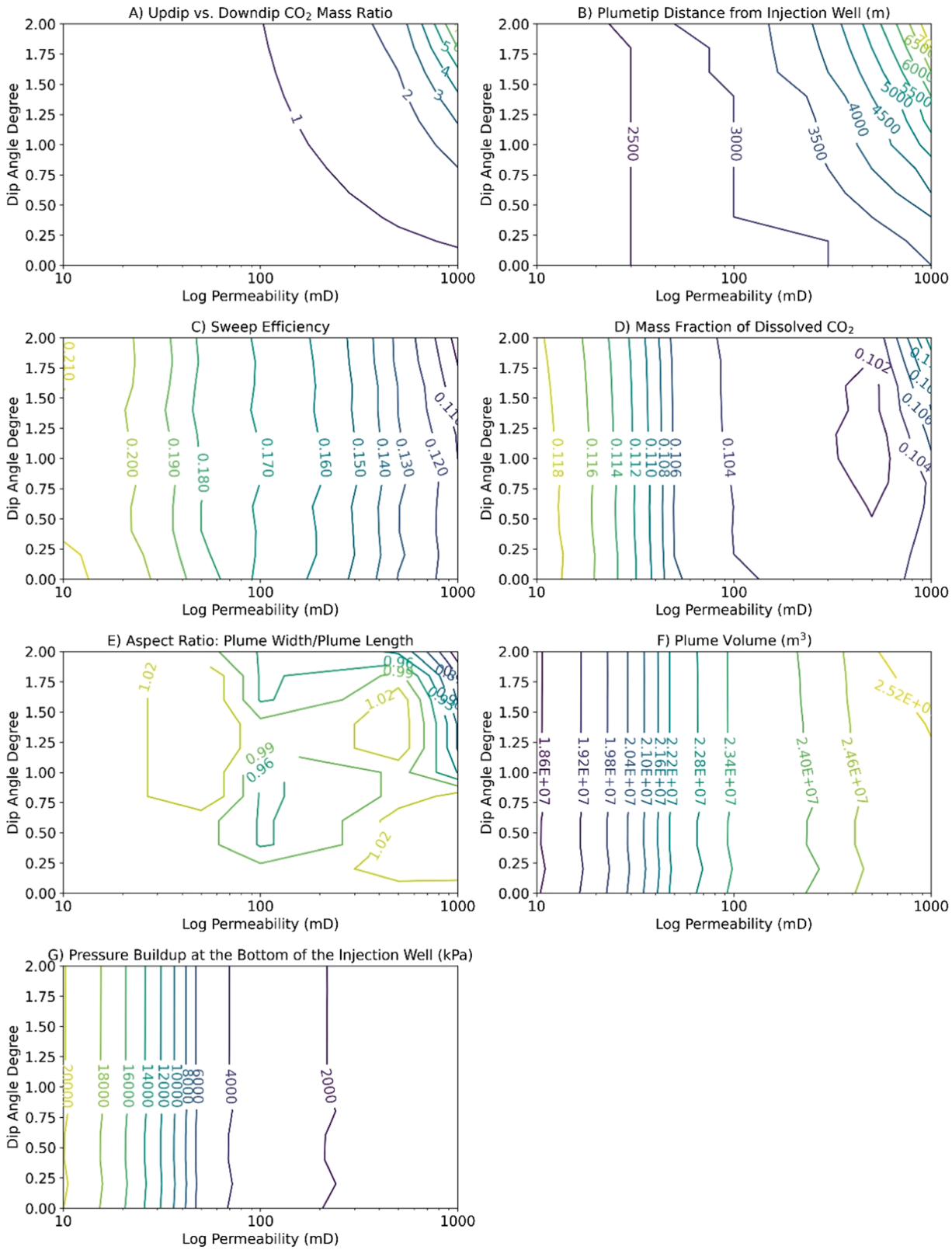

Fig. 2. A. Up-dip versus down-dip CO_2 mass ratio at the end of injection as a function of permeability and dip angle. B. Plume tip distance from the injection well at the end of injection as a function of permeability and dip angle. C. Sweep efficiency at the end of injection as a function of permeability and dip angle. D. Mass fraction of dissolved CO_2 at the end of injection as a function of permeability and dip angle. E. Plume aspect ratio is defined as plume width divided by plume length at the end of injection as a function of permeability and dip angle. F. Plume volume, m^3, at the end of injection as a function of permeability and dip angle. G. Pressure buildup at the bottom of the injection well in kPa at the end of injection as a function of permeability and dip angle.

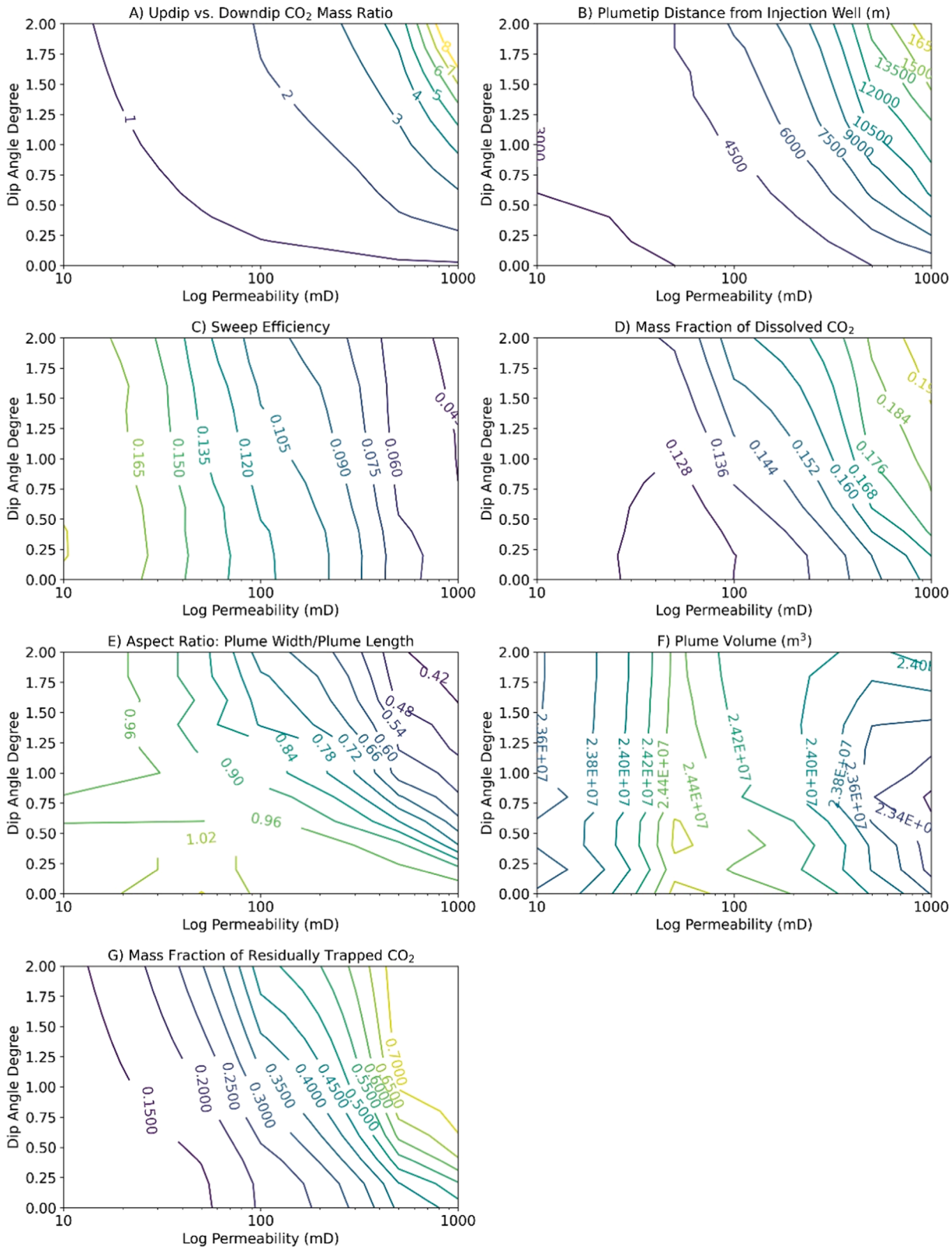

Fig. 3. A. Up-dip versus down-dip CO_2 Mass Ratio 100 years post-injection as a function of permeability and dip angle. B. Plume tip distance from the injection well 100 years post-injection as a function of permeability and dip angle. C. Sweep efficiency 100 years post-injection as a function of permeability and dip angle. D. Mass fraction of dissolved CO_2 100 years post-injection as a function of permeability and dip angle. E. Plume aspect ratio is defined as plume width divided by plume length 100 years post-injection as a function of permeability and dip angle. F. Plume volume, m^3, 100 years post-injection as a function of permeability and dip angle. G. Mass fraction of residually trapped CO_2 100 years post-injection as a function of permeability and dip angle.

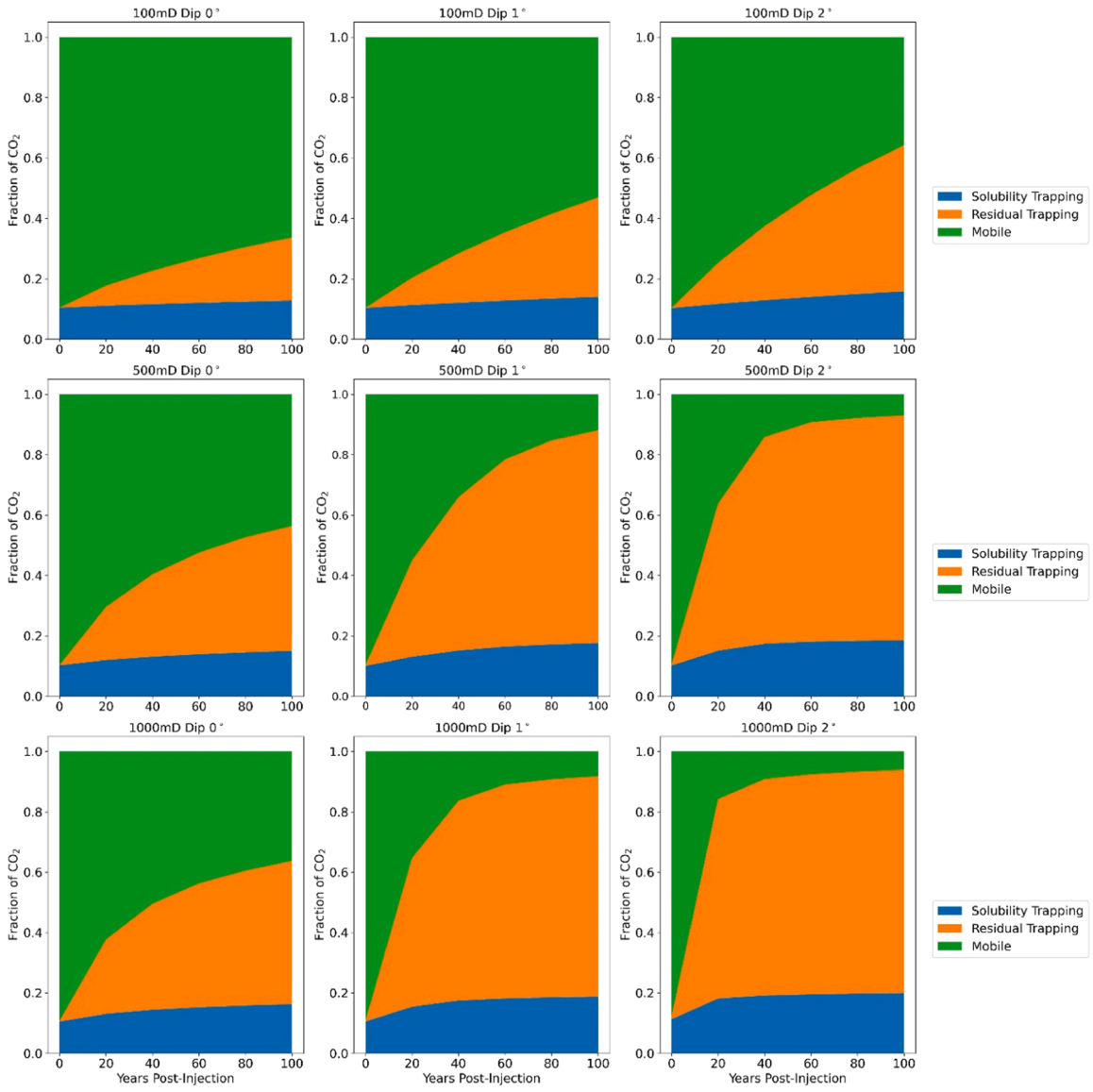

Fig. 4. The mass fraction of the CO_2 plume dissolved in the brine, residually trapped and mobile free phase for permeabilities = 100mD, 500mD, 1000mD and dips of 0°, 1° and 2° from the end of injection to 100 years post-injection.

Table 2
For a given dip, there are five interacting factors that influence the supercritical phase CO_2 plume volume behavior.

Interacting Factors	Impact on CO_2 Plume Volume
① CO_2 Saturation	Increasing the CO_2 saturation, decreases the plume volume
② Solubility Trapping	Increasing solubility trapping, decreases the plume volume
③ Residual Trapping	Increasing residual trapping, decreases the plume volume
④ CO_2 Density	Increasing the CO_2 density, decreases the plume volume
⑤ Permeability	Increasing the permeability, increases the plume volume during injection

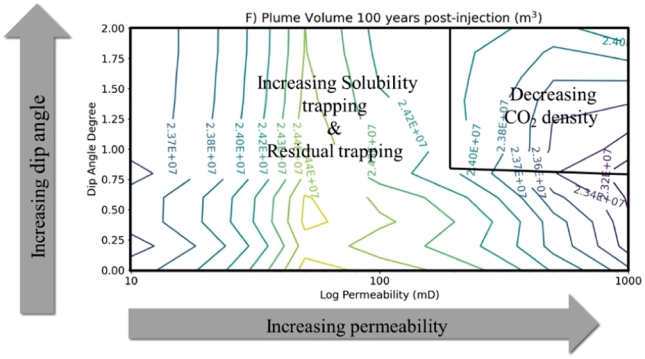

Fig. 5. Five interacting factors that influence plume volume 100 years post-injection. Two regimes can be identified with residual trapping, solubility trapping, and CO_2 density as driving forces behind plume volume behavior.

post-injection. The injection well is located near the center and is perforated in the bottommost 12 m of the reservoir. Brooks-Corey constitutive relations for relative permeability and capillary pressure were used (Brooks and Corey, 1964). Details for the relative permeability and capillary pressure curves can be found in Appendix C. The Land trapping model was used to calculate the amount of residual trapping (Land, 1968). The dip of the reservoir varied between 0° and 2°

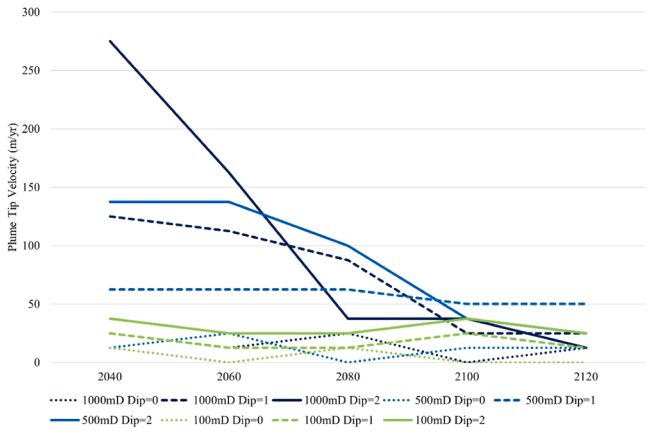

Fig. 6. Velocity of CO_2 plume in the post-injection period.

in 0.2° increments. A maximum reservoir dip of 2° was chosen to examine almost flat reservoirs that are unbounded and see the impact of small dip angles. Dimensionless gravity numbers vary from 0.015 to 1.67 and the capillary numbers are on average on the order of 10^{-10}, so capillary forces dominate (Appendix D Tables D.2 and D.3). The permeability ranged from 10mD to 1,000mD with a k_v/k_h ratio of 1. The porosity was set to 0.15 and salinity was 30,000 mg/L. This salinity value was chosen to be representative of the formation fluid in offshore sediments which is typically similar to sea water (Litynski et al., 2011).

3. Results

3.1. Plume migration

To estimate the extent of the up-dip plume migration, the mass of CO_2 in the gas phase and dissolved in the brine that migrated up-dip from the injection well was calculated and compared to the mass of CO_2 dissolved and free-phase that migrated down-dip from the injection well. Fig. 2A shows this ratio at the end of the 20-year injection period for varying permeabilities and dip angles. For permeabilities less than 200 mD, the ratio between up-dip CO_2 mass and down-dip mass remains unity for all dip angles between 0° and 2°. This indicates that the plume is symmetric in the x-direction about the injection well. However, as the permeability and dip angle increase, more CO_2 migrates up-dip, up to 6x more in the 1000 mD and 2° dip case. One hundred years post-injection, this trend becomes amplified (Fig. 3A). In the highest permeability and dip case, 8x more CO_2 mass is up-dip versus down-dip.

The plume tip distance is the maximum distance the plume has migrated up-dip away from the injection well. At the end of injection, for low permeabilities, the plume tip distance remains constant for increasing dip angles (Fig. 2B). As the permeability increases, the plume tip distance increases with increasing dip. For a 1000 mD reservoir, a flat reservoir would have a plume radius of about 3,500 m away from the injection well. This distance increases to 7000 m for a 2°dip reservoir. After 100 years, the plume has continued to migrate away from the injection well (Fig. 3B). In low permeability reservoirs, the plume tip distance has increased from 2,500 m to 3,000 m and remains constant for all dip angles. However, as permeability increases, the distance the plume migrates up-dip increases significantly in the post-injection period. In the case of a 1000 mD flat reservoir, the plume tip has migrated about 6,000 m away from the injection well and in a 2°reservoir, this distance increases to 16,500 m.

3.2. Sweep efficiency

The sweep efficiency is a measure of how efficiently the storage space in a reservoir is used and is given by Eq. (1). For the same amount of injected CO_2, a greater sweep efficiency indicates a smaller plume footprint and a lesser sweep efficiency results in a larger plume footprint (Van der Meer, 1995). The footprint is the areal extent of the plume, that is the area of the plume in the topmost layer in the z-direction.

$$E_{sweep} = \frac{V_{gas}}{V_{r_{footprint}}} = \frac{\sum_n V_n \phi_n S_n}{\sum_{nefootprint} V_n \phi_n} \quad (1)$$

where V is the cell volume, ϕ is the porosity, S is the average gas saturation, n denotes the spatial grid cell, and $n \in footprint$ denotes all grid cells within the plume footprint (Wen et al., 2021). In Fig. 2C, the sweep efficiency varies from 0.2 to 0.1. These values remain fairly constant for varying dips for permeabilities below 800mD. A hundred years post-injection, sweep efficiency values have decreased to 0.165 for low permeabilities and 0.045 for high permeabilities

(Fig. 3C). This decrease in sweep efficiencies is greater for high permeabilities as the plume footprint increases post-injection significantly.

3.3. Plume shape and volume

In homogeneous reservoirs, the CO_2 plume shape from an aerial view changes from circular in flat reservoirs to more oblong as the plume migrates further in the up-dip direction (Appendix E, Figs. E.1–E.6). To characterize this change in shape, the aspect ratio is calculated. The aspect ratio measures the ratio of the CO_2 plume width to the length of the plume (Fig. 2E). An aspect ratio of one reflects a circular plume shape in the x- and y-direction. A ratio higher than one indicates that the plume width (y-direction) is greater than the plume length (x-direction). Conversely, a ratio of less than one indicates that the plume length is greater than the width. In Fig. 2E, low permeabilities tend to have aspect ratios around one for all dip angles at the end of injection. Similarly, the aspect ratio tends to be around one for all permeabilities with dip angles less than 1°. For permeabilities above 600mD with dip angles greater than 1°, the aspect ratio begins to decrease to 0.80, indicating a CO_2 plume width that is 0.8x the plume length. One hundred years post-injection, all permeabilities and dips greater than 0° have an aspect ratio less than one as the plume spreads up-dip (Fig. 3E).

The plume volume uses the total CO_2 in the gas phase. The plume volume at the end of injection increases with increasing permeability and in cases with a permeability greater than 500mD, the plume volume also increases with increasing dip angle (Fig. 2F). One hundred years post-injection, the plume volume decreases with increasing permeability. For permeabilities greater than 500mD, the plume volume decreases from 0°to about 1°then increases for dip angles greater than 1° (Fig. 3F).

3.4. Secondary trapping

The amount of CO_2 dissolved in brine increases as the plume migrates up-dip, particularly in high permeability and high dip cases (Fig. 2D). At the end of injection, the mass fraction of dissolved CO_2 ranges from 0.102 to 0.110. Low permeabilities have relatively constant amounts of dissolved CO_2 for all dip angles. The increase is due to the increase in CO_2 solubility in brine that occurs as pressure increases in these low permeability reservoirs (Fig. 2G). At higher permeabilities, the amount of dissolved CO_2 increases with increasing dip angle as the plume migrates further up-dip, exposing free-phase CO_2 to more undersaturated brine. In the post-injection period, residual trapping is the dominant trapping process (Fig. 4). In Fig. 4, the total amount of CO_2 injected is divided into the dissolved phase, immobile, and mobile portions. Throughout injection, about 10% of the CO_2 dissolves into the brine and the rest of the injection CO_2 is mobile. Once injection stops, the fraction of CO_2 dissolved increases in all cases, ranging from 0.128 to 0.192 (Fig. 3D). The amount of CO_2 residually trapped ranges from 0.15 to 0.7 (Fig. 3G). Below 100mD, the amount of residually trapped CO_2

stays constant over dip angles from 0° to 2°. Above 100mD, the amount of residually trapped CO_2 increases with increasing dip angle and a maximum is reached around 500mD and 1° dip. Over 100 years post-injection, solubility and residual trapping can immobilize anywhere from 27.8% to 89.2% of the CO_2 plume.

3.5. Pressure buildup

Another important factor to consider when selecting a suitable storage site is the pressure buildup when injecting CO_2. Fig. 2G shows the pressure buildup for a range of permeability and dip angles. This figure shows that the pressure buildup does not vary much with dip angle but does decrease with increasing permeability. Injecting 1 MT/yr into a 10mD reservoir results in a pressure buildup 100% of the initial reservoir pressure and exceed the fracture pressure. The pressure buildup for a 50mD, 100mD, 500mD, and 1,000mD reservoir are 25%, 13%, 3%, and 1% the initial reservoir pressure, respectively. Limiting the pressure buildup to 50–75% of the initial reservoir pressure, for these 40 m thick cases, reservoirs with a permeability above 50mD would be suitable based on the pressure buildup.

4. Discussion

The findings presented in this work are useful to inform site selection for carbon storage in unbounded saline aquifers. In Section 3.1, the simulations of plume migration in dipping reservoirs show that the migration of CO_2 is strongly dependent on the reservoir dip angle in high permeability reservoirs. The ability to estimate the extent of up-dip migration can be important in the site selection process to avoid sites that may have hazards up-dip that could become potential leakage pathways, in addition, to informing the monitoring area and monitoring well placement.

From the results presented in the previous section, for a given reservoir dip angle, five interacting factors have been identified that control the mobile gas-phase CO_2 plume volume: CO_2 saturation, solubility trapping, residual trapping, CO_2 density, and permeability (Table 2). The saturation of a fluid is defined as the fraction of the pore space occupied by that fluid. All else being equal, increasing the average CO_2 saturation of the plume also increases the sweep efficiency (Eq. (1)), thereby resulting in a smaller plume footprint as the pore space is utilized more efficiently. With larger CO_2 saturation in the pore space, the amount of dissolution of CO_2 into the brine is decreased because there is less water available in the pore space to dissolve CO_2. In contrast, as the saturation of the CO_2 increases, the saturation of the residually trapped CO_2 can increase towards the maximum non-wetting residual saturation, S_{nwrmax}, thus, increasing the amount of CO_2 residually trapped in the pores (Kumar et al., 2004).

Both solubility trapping and residual trapping also decrease the mobile free-phase plume volume. In Section 3.4, the amount of trapped CO_2 is quantified through residual trapping and solubility trapping and shows that both increase with increasing permeability and dip angle. Residual trapping is the dominant trapping mechanism in the post-injection period. Residual trapping occurs during the imbibition process as the water saturation increases and CO_2 becomes trapped in the pore space. Most of the plume is undergoing the drainage process just after injection ends, apart from a narrow imbibition zone at the plume's trailing edge (Doughty, 2010; Juanes et al., 2010). The imbibition zone increases during the post-injection period until about 60 years in the higher permeability and dip cases when drainage is limited to the leading edge of the plume. Immobilizing the plume is beneficial as it increases storage security and decreases plume migration.

As the plume migrates up-dip, particularly for high permeability reservoirs, the density of the CO_2 plume decreases as pressure decreases. As the plume approaches the supercritical point for CO_2, typically around 800 m below the surface, the density decreases substantially as CO_2 transitions from a supercritical fluid to a gas. This decrease in CO_2 density expands the plume volume as the CO_2 migrates up-dip from the injection well.

Lastly, reservoir permeability has a strong influence on the plume volume and plume migration. As the reservoir permeability increases, the CO_2 plume moves further in the reservoir due to buoyancy and can migrate further up-dip in the case of a dipping reservoir. During injection, the plume volume increases with increasing reservoir permeability.

These factors can be applied to Fig. 3F to understand the driving factors behind the behavior of the plume volume with increasing permeability and dip angle. Two regimes can be identified that are driven by the change in solubility trapping, residual trapping, and CO_2 phase density (Fig. 5).

On the left-hand side and bottom right-hand corner of Fig. 5, the decrease in the plume volume is due to an increase in solubility trapping and an increase in residual trapping. However, in the upper right-hand corner, the decrease in CO_2 density as it migrates toward the surface is the driving force for the increase in plume volume that is seen for high permeability reservoirs with dips between 1° and 2°. Understanding the forces behind the change in plume volume during the post-injection period informs the desired reservoir characteristics for a particular project, thus aiding the site selection process.

4.1. Influence of pore distribution parameter, λ, on P_c

The pore distribution parameter, λ in the Brooks-Corey capillary pressure curves impacts the results (Eq. C.1, Eq. C.2). The base case uses a λ of 0.6, that represents a wide range in pore sizes and has a similar shape to the capillary pressure curves presented in the work of (Pini and Benson, 2017) for a Berea sandstone core. To understand the impact of the pore-size distribution parameter, λ was increased to 2 and decreased to 0.4 (Fig. C.1). Increasing λ to 2 represents a rock with a more uniform range of pore sizes and looks similar to the shape of the capillary pressure curve for glass beads from (Brooks and Corey, 1964). A λ of 2 has a flatter capillary pressure drainage curve than the base case indicating more homogeneity in pore sizes, which results in more plume migration up-dip and larger plume volumes than the base case in dipping reservoirs. There is no figure illustrating this impact from λ in this work. The plume tip distance from the injection well is between 28% and 43% greater at the end of injection due to the increase in λ and sweep efficiencies are smaller. CO_2 saturations are larger, resulting in less dissolution as there is less water in the pore space to dissolve the CO_2. However, with the larger CO_2 saturations, more residual trapping can occur. This combination of less solubility trapping and more residual trapping changes Fig. 3F by increasing the plume volume and shifting the "C-shaped" trend where plume volumes decrease then increase to smaller permeabilities. Conversely, in the case with a smaller λ, a larger increase in capillary pressure is needed to achieve large CO_2 saturations, so the plume experiences smaller CO_2 saturations, resulting in increased solubility trapping and decreased residual trapping. This results in lower plume volumes and a smoother and shifted right-hand side of Fig. 3F.

4.2. Impact of maximum non-wetting residual saturation

A sensitivity study was performed to investigate the impact of the maximum residual non-wetting saturation, S_{nwrmax}. Without residual trapping, the CO_2 plume will rise to the top of the reservoir and spread out. In many cases, CO_2 acts as the non-wetting phase when injected in a saline reservoir and can become trapped during imbibition (M.A. Hesse, 2008; Krevor et al., 2015). The base case analysis used a S_{nwrmax} of 0.4. This value varied from 0.2 to 0.3. As S_{nwrmax} increases, the amount of residual trapping also increases (Fig. B.1 in Appendix B). In the 100mD reservoir, the fraction of CO_2 residually trapped increases from about 0.1 to 0.2 in a flat reservoir, 0.15 to 0.25 in a 1° dip reservoir, and 0.2 to 0.5 in a 2° dip reservoir. Increasing the reservoir permeability increases the initial amount of trapping and the percent increase with increasing S_{nwrmax}.

4.3. Plume front velocity and stabilization time

Because many of these sloping regional saline storage formations do not have structural closure, potentially leading to leakage from up-dip migration, the speed of the CO_2 plume front and stabilization time needs to be considered (Chadwick et al., 2008; M.A. Hesse, 2008; Hesse et al., 2006). The velocity of the plume front for each time step in the post-injection time frame was calculated (Fig. 6). In Fig. 6, reservoirs with permeabilities of 100 mD, 500 mD, and 1000 mD and dip angles of 0°, 1°, and 2° are shown. The only case in the nine cases presented that the plume stabilizes is the flat 100mD reservoir. However, in the more permeable cases, it is notable that most of the movement occurs in the first forty to sixty years. The largest movement is experienced in the case of the 1000 mD reservoir with a 2° dip angle where the plume tip distance doubles in the first forty years, then the velocity of the plume significantly reduces and begins to level out. From Fig. 4, the driving force behind the decrease in velocity becomes apparent: the rate and amount of residual trapping. For 100 mD reservoirs, the residual trapping gradually increases. However, in the more permeable cases, there is a significant increase in the amount of residually trapped CO_2 in the first sixty years for 500 mD reservoirs and in the first forty years for 1000 mD reservoirs.

The results are for reservoirs with a specific depth, salinity, and thickness however these findings can be applied more broadly to dipping reservoirs with different reservoir properties. Deeper reservoirs will have higher CO_2 density, that will result in a more compact plume and less lateral migration and higher sweep efficiency. This model uses salinity typical for offshore environments. As the salinity of the brine increases, the solubility of the CO_2 decreases, which reduces the amount of solubility trapping (Enick and Klara, 1990). The mobility ratio also decreases as the salinity of the brine increases, resulting in less CO_2 invading the pore space and less residual trapping (Brennan, 2014). The reservoir thickness influences the injectivity and pressure buildup. In particular, for the low permeability reservoirs, a smaller pressure buildup reduces the amount of solubility trapping. Looking at the dimensionless gravity number (Eq. D.1 in Appendix D), increasing the thickness increases the buoyancy force. This work studies isotropic reservoirs and future studies will examine the impact of anisotropy. However, for reservoirs with a $k_v/k_h \leq 0.1$, we would expect higher sweep efficiencies and a more compact plume.

5. Conclusion and future work

This study focuses on modeling CO_2 storage in 3D dipping unbounded saline reservoirs. By systematically investigating a range of permeabilities and dip angles using numerical simulations, we quantify the relationship among secondary trapping, plume migration, reservoir dip angle, and permeability. We found that one hundred years post-injection, up to 8x more CO_2 mass can migrate up-dip versus downdip and that the plume tip can migrate up to 16,500 m up-dip from the injection well. This migration is offset by an increase in solubility and residual trapping with increases in dip angle and 30% to 90% of the CO_2 plume can be immobilized in the post-injection period. The residual trapping rate and the amount is the driving force behind decreasing the CO_2 plume velocity. Although additional simulation time was needed to determine the stabilization time for high permeability reservoirs, most of the plume movement takes place in the first forty to sixty years after the end of injection. Five key parameters control the plume volume in dipping reservoirs: CO_2 saturation, residual saturation of CO_2 solubility in brine, permeability, and CO_2 density. Sensitivity to the pore distribution factor and the maximum non-wetting residual saturation influence the results by changing the interaction between the five key parameters identified.

Using these findings, we determine the optimal permeability and dip angle combination to maximize the amount of secondary trapping and minimize the amount of plume migration. However, we cannot examine dip angle independent of permeability. To be distinguished from previous studies, the novelty of this work comes from the systematic approach of investigating a range of dip angles and permeabilities and examining the sensitivity of the findings to factors such as the pore distribution parameters and the maximum non-wetting residual saturation. Additional assumptions made during the simulations, such as the depth of the injection well and salinity, will impact the results. This study does not examine any potential viscous fingering that occurs at the CO_2-water interface along the top of the reservoir as it is beyond the scope of this paper. The results of this analysis are for a homogeneous reservoir and the next steps will include incorporating the impact of heterogeneity and permeability anisotropy on CO_2 plume migration and trapping in saline reservoirs. These results can be incorporated into the site selection process to find an optimal CO_2 storage saline reservoir as well as initial planning for spatial extent of monitoring as illustrated elsewhere (Callas et al., 2023).

CRediT authorship contribution statement

Catherine Callas: Conceptualization, Methodology, Investigation, Writing – original draft, Writing – review & editing, Visualization. **Anthony R. Kovscek:** Supervision, Writing – review & editing. **Sally M. Benson:** Supervision, Funding acquisition.

Declaration of Competing Interest

The authors declare the following financial interests/personal relationships which may be considered as potential competing interests: Catherine Callas reports financial support was provided by ExxonMobil Corp.

Data availability

Data will be made available on request.

Acknowledgment

This work was supported by ExxonMobil through the Strategic Energy Alliance at Stanford University and the Stanford Center for Carbon Storage.

Appendix A. Grid selection

A grid sensitivity study was performed because plume migration and mass fraction of CO_2 dissolved are sensitive to cell size ((Yamamoto and Doughty, 2011). In the x-direction, we performed a sensitivity study with grid cell widths of 100 m, 250 m, 300 m, 400 m, and 500 m cells in the region the plume is located. The cross-section of a flat 1000 mD reservoir is displayed in Fig. A.1 with a range of grid widths. The plume edge becomes more refined with finer grid blocks. The estimated plume tip distance difference between the 100 m and 250 m grid cell size is approximately 2%.

The plume tip distance, aspect ratio, sweep efficiency, plume volume, up-dip vs downdip CO_2 mass ratio and mass fraction of dissolved CO_2 are shown for a 1000 mD reservoir 100 years post-injection for varying grid block sizes (Fig. A.2). These figures show reservoirs with dip angles of 0°, 1°, and 2° From this figure, metrics like plume volume and mass fraction of dissolved CO_2 level out around 250 m to 300 m grid block sizes. Other metrics

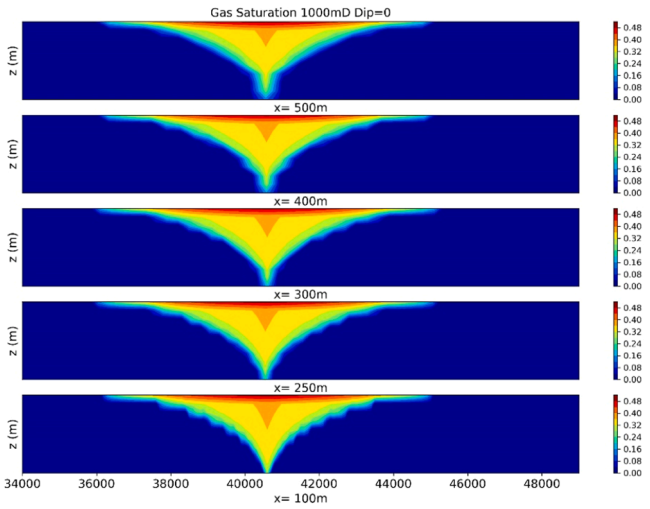

Fig. A.1. Comparison of the supercritical CO_2 saturation cross-section of a flat 1000 mD reservoir with varying cell widths in the x-direction 100 years post-injection.

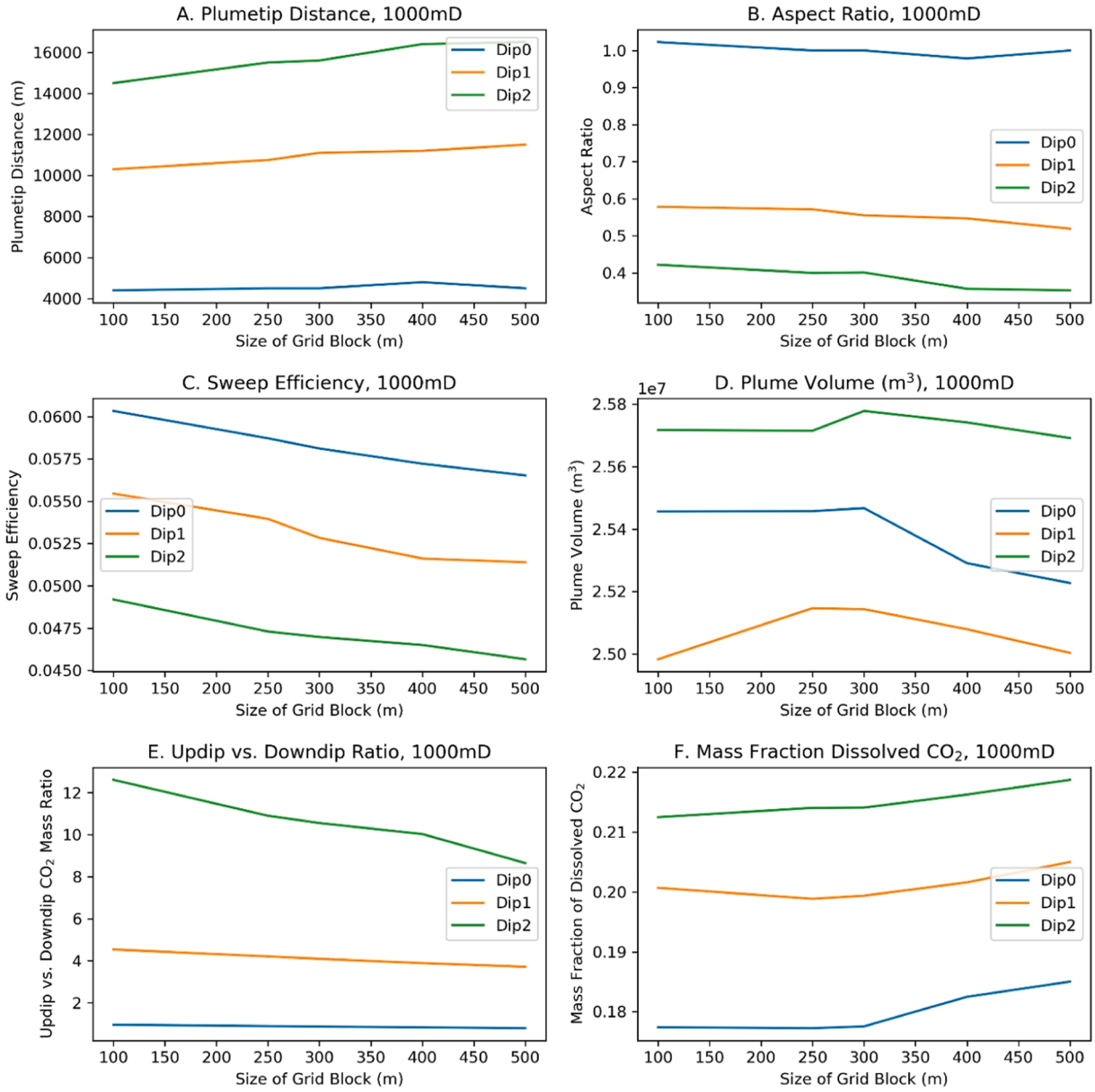

Fig. A.2. Comparison of the different metrics for a 1000 mD reservoir with varying cell widths in the x-direction 100 years post-injection.

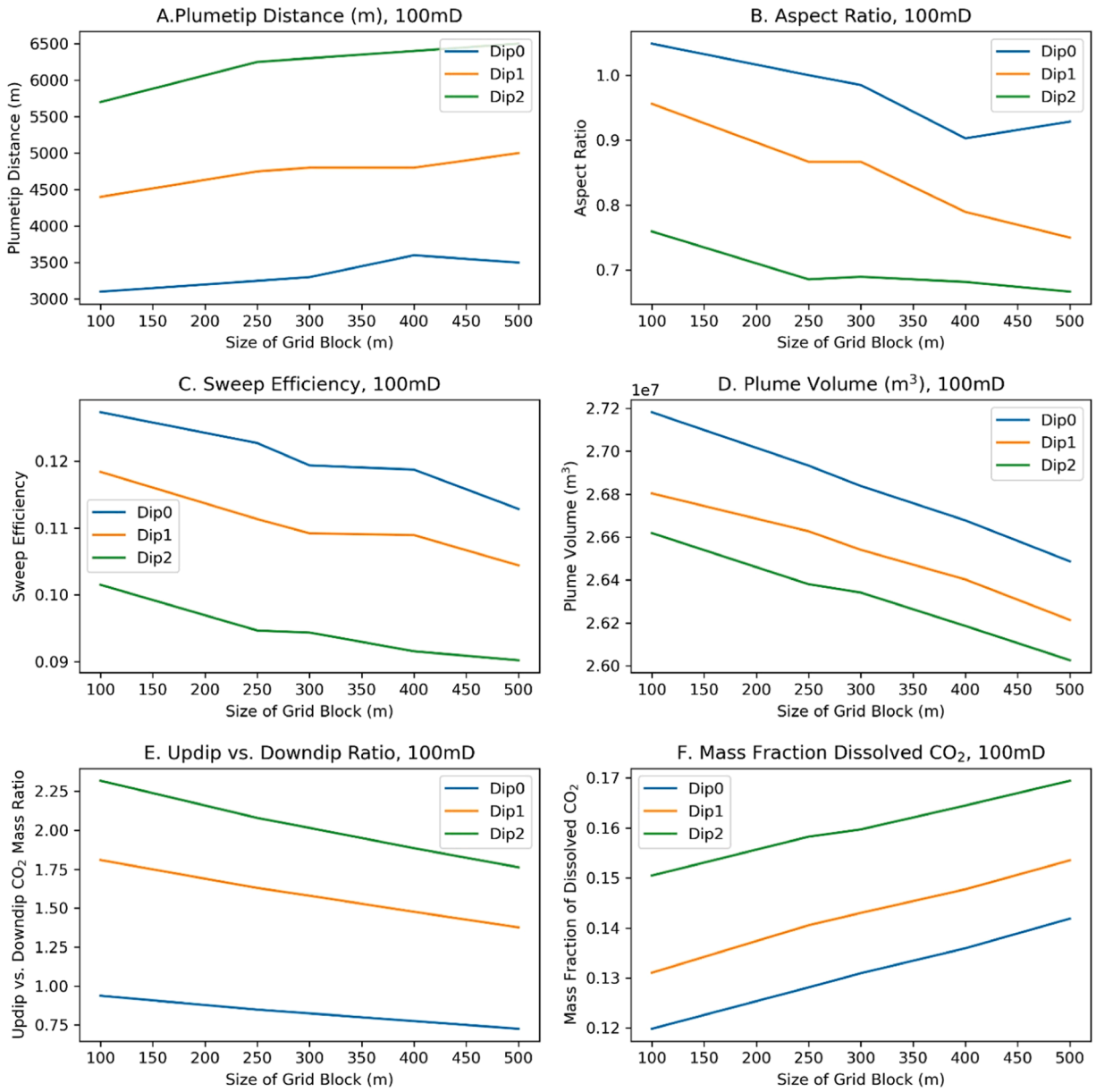

Fig. A.3. Comparison of the different metrics for a 100 mD reservoir with varying cell widths in the x-direction 100 years post-injection.

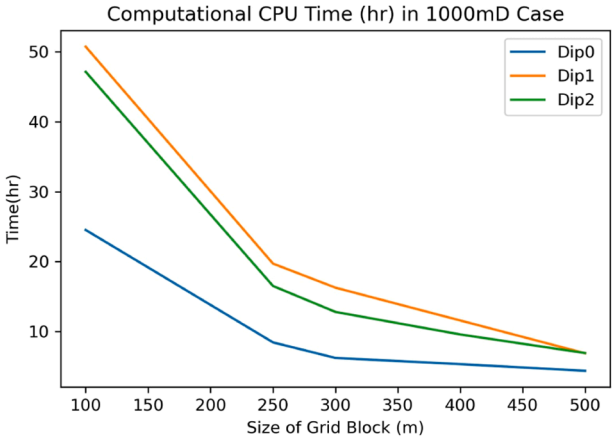

Fig. A.4. Computational time to run simulations with varying cell widths in the x-direction 100 years post-injection.

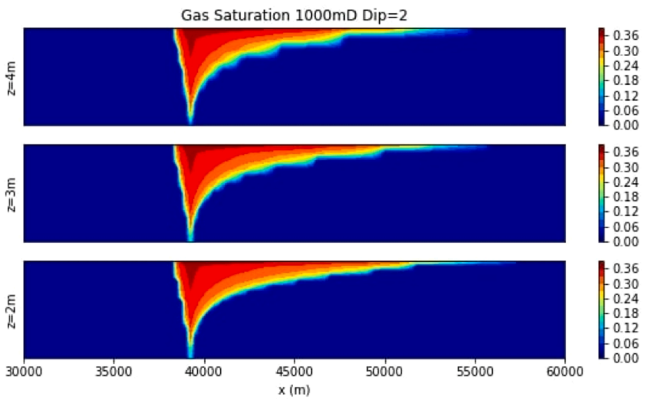

Fig. A.5. Comparison of the supercritical CO_2 saturation cross-section of a 2°dip 1000 mD reservoir with varying cell thicknesses in the z-direction 100 years post-injection.

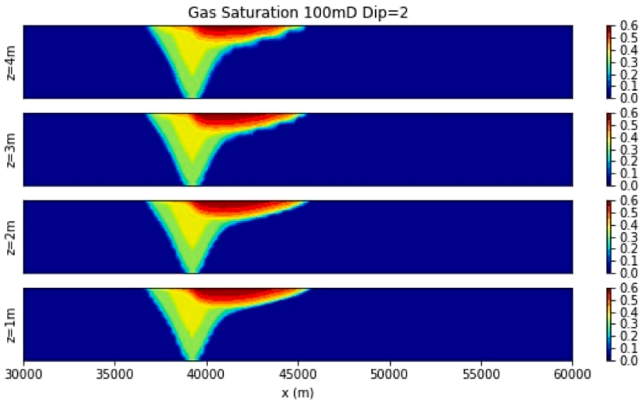

Fig. A.6. Comparison of the supercritical CO_2 saturation cross-section of a 2°dip 100mD reservoir with varying cell thicknesses in the z-direction 100 years post-injection.

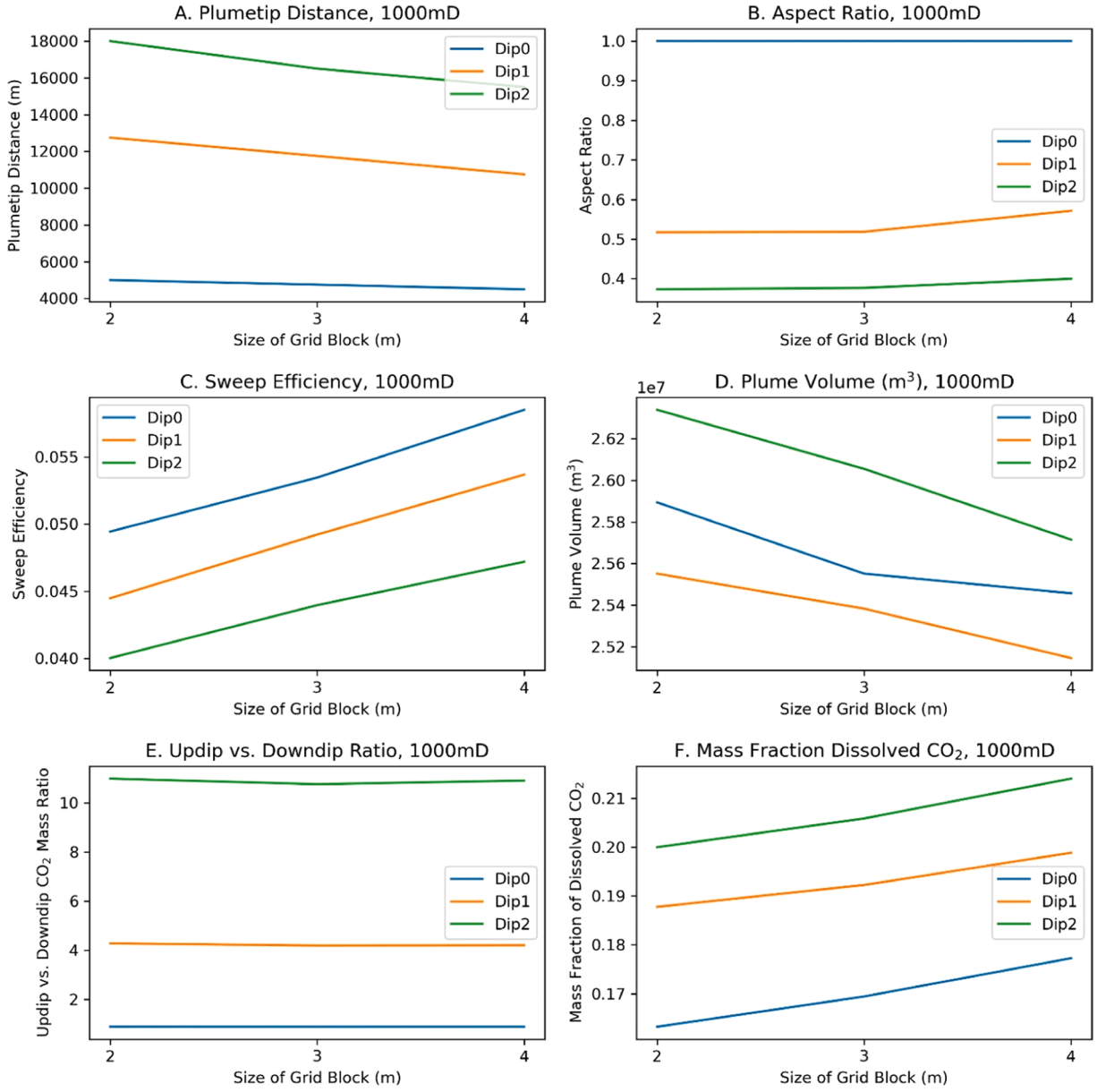

Fig. A.7. Comparison of the different metrics for a 1000 mD reservoir with varying cell widths in the z-direction 100 years post-injection.

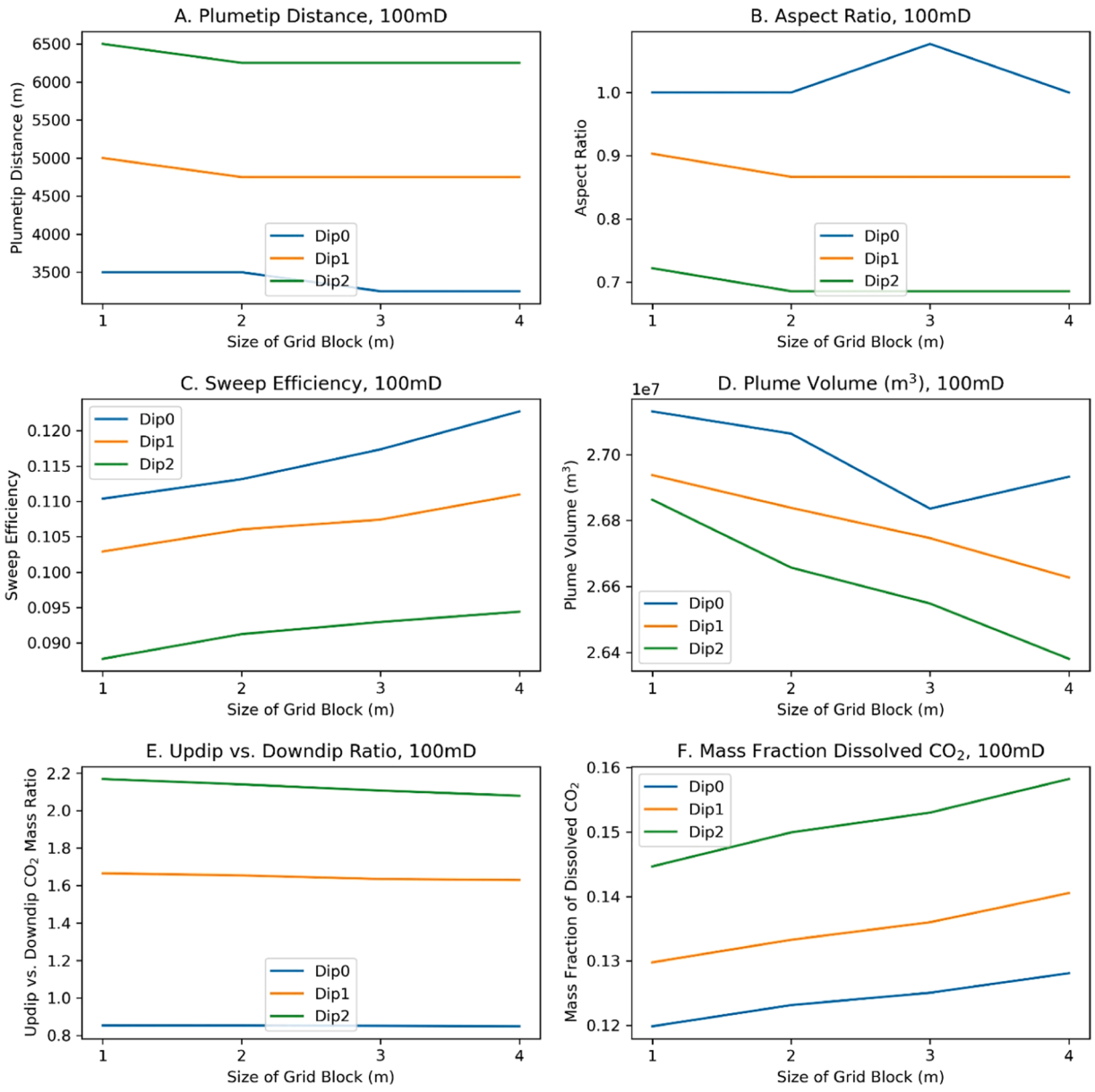

Fig. A.8. Comparison of the different metrics for a 100 mD reservoir with varying cell widths in the z-direction 100 years post-injection.

like up-dip vs downdip ratio for lower dip reservoirs change very little with varying grid block sizes. Fig. A.3 shows these same metrics for a 100 mD reservoir 100 years post-injection. The parameters in A.3 do not show a leveling off with finer grid sizes even down to 100 m grid block size, which indicates that finer grid size is needed. However, the CPU time limits the ability to perform studies finer than 100 m and the computational time significantly increases at grid block sizes less than 250 m (Fig. A.4). The computational time significantly increases from a 250 m grid cell width to a 100 m width. Therefore, we chose a 250 m grid width size in the x-direction to achieve the most refined results while balancing the computational demands of running these simulations.

In the vertical direction, the cell thicknesses examined were 2, 3, and 4 m. A cross-section of the CO_2 saturation for a 1000 mD and 100 mD reservoir with a dip of 2° are displayed in Figs. A.5 and A.6. In both cases, decreasing the grid cell thickness increases the plume detail. However, in the 1000 mD 2° dip case, there is a 14% difference in the plume tip distance for a grid cell thickness of 4 m compared to 2 m. In contrast, in the 100 mD 2° dip reservoir, the difference in plume tip distance is only 4% between the 4 m and 2 m grid cell thicknesses. We also examined the aspect ratio, sweep efficiency, plume volume, up-dip vs downdip CO2 mass ratio, and mass fraction of dissolved CO_2 for a 1000 mD and a 100 mD reservoirs (Figs. A.7 and A.8). Therefore, we decided to use 2 m grid cell thicknesses for the 500 mD and 1000 mD reservoirs to decrease the error stemming from the grid cell size. For cases with permeabilities less than 100 mD, we chose to use 4 m grid cell thicknesses because the error is less than 4%.

Appendix B. Varying S_{nwrmax}

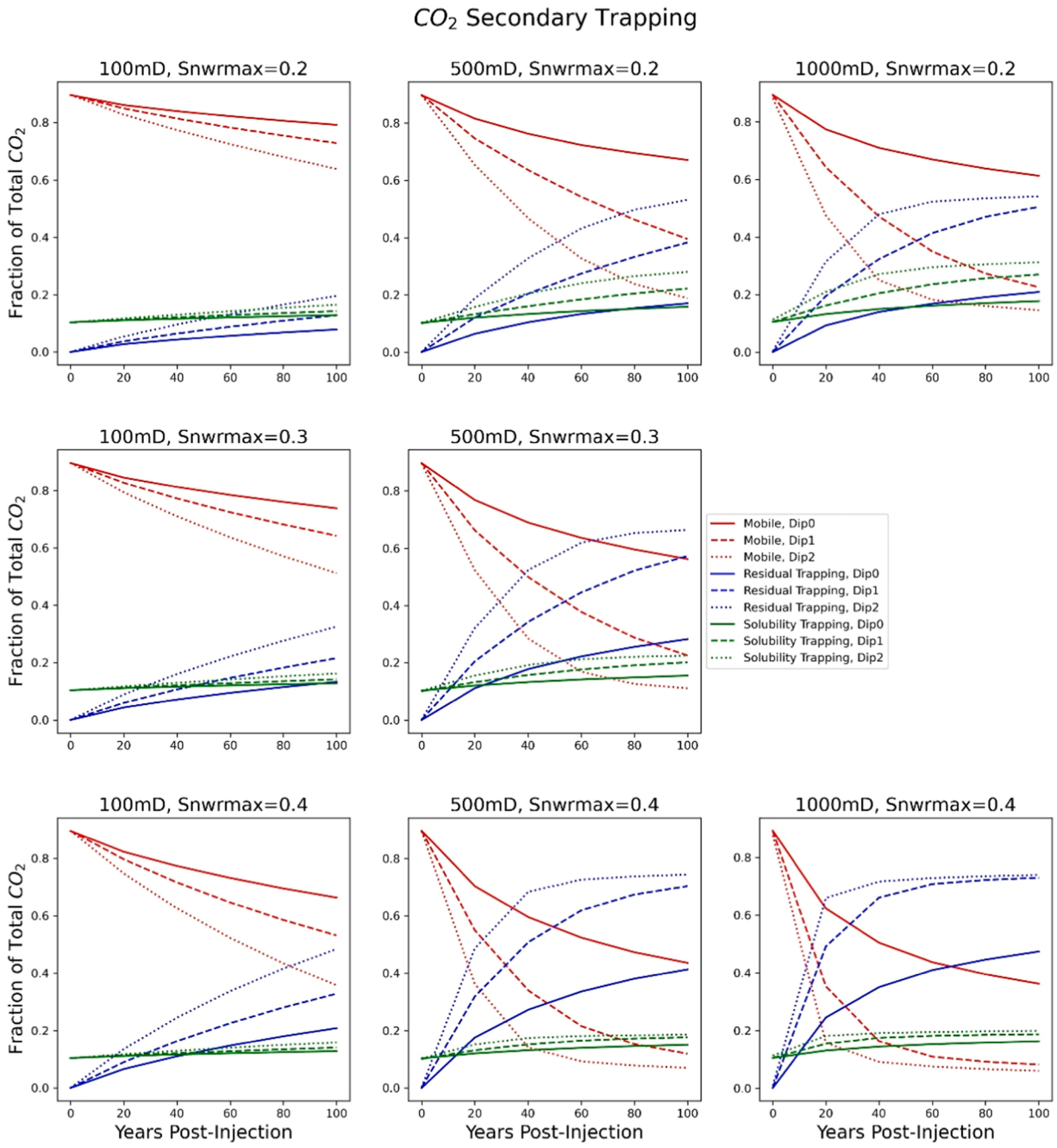

Fig. B.1. Fraction of CO_2 post-injection dissolved in brine, residually trapped and mobile for varying S_{nwrmax} in a 100 mD, 500 mD, and 1000 mD reservoir for reservoirs with 0°, 1°, and 2° dip angle.

Appendix C. Brooks-Corey parameters

The Brooks-Corey model for capillary pressure, P_c, curves for drainage and imbibition:

$$P_{CD} = P_e \left(\frac{S_w - S_{w_{irr}}}{1 - S_{w_{irr}}} \right)^{\frac{-1}{\lambda}} \tag{C.1}$$

$$P_{C_I} = P_e \left(S_{w,\ eff}^{\frac{-1}{\lambda}} - 1 \right) \tag{C.2}$$

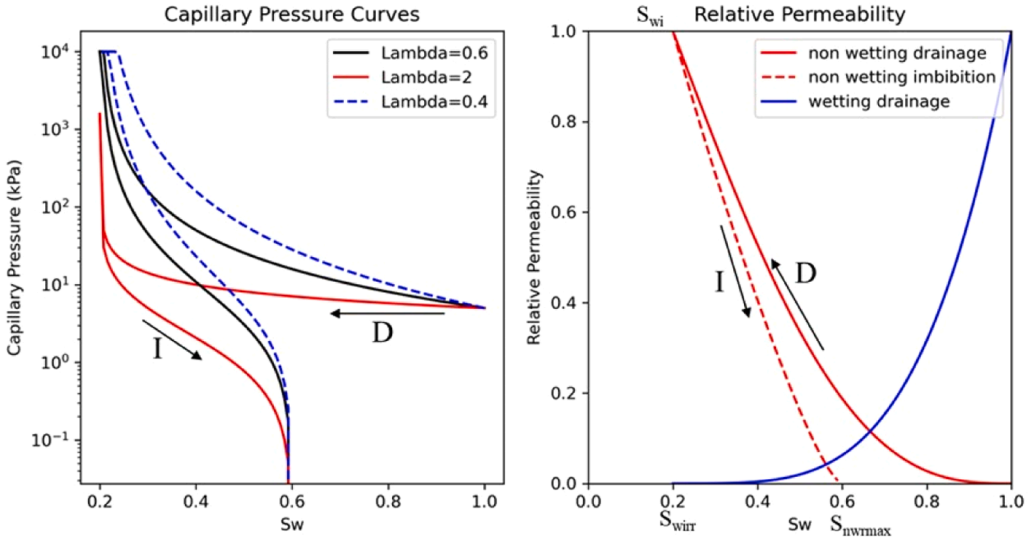

Fig. C.1. : Capillary pressure curves and relative permeability curves using Brooks-Corey equations used in these simulations. The drainage curve is indicated with a D and the imbibition curve is indicated with an I.

where P_e is the capillary entry pressure, $S_{w_{irr}}$ is the irreducible wetting phase saturation, S_w is the wetting phase saturation, λ is the pore distribution parameter, and $S_{w,eff} = \frac{S_w - S_{w_{irr}}}{1 - S_{w_{irr}} - S_{nwrmax}}$.

The Brooks-Corey model for drainage relative permeability for the wetting and non-wetting phase used is given below:

$$k_{rw_D} = \left(S_w^*\right)^{\frac{2}{\lambda}+3} \tag{C.3}$$

$$k_{rnw_D} = k_{rnw}(S_{w_i}) * \left(1 - S_w^*\right)^2 * \left(1 - \left(S_w^*\right)^{\frac{2}{\lambda}+1}\right) \tag{C.4}$$

where λ is 2 and $S_w^* = \frac{S_w - S_{w_i}}{1 - S_{w_i}} = 1 - S_{nw}^*$ and S_{w_i} is the wetting phase saturation at the start of imbibition. The imbibition relative permeability for the non-wetting phase is expressed as

$$k_{rnw_I} = k_{rnw_D}(S_{w_i}) * \left(S_{nwf}^*\right)^2 * \left(1 - \left(1 - S_{nwf}^*\right)^{\frac{2}{\lambda}+1}\right) \tag{C.3}$$

where S_{nwf} is the flowing non-wetting phase saturation that is written as

$$S_{nwf}^* = 0.5 * \left(\left(S_{nw}^* - S_{nwr}^*\right) + \sqrt{\left(S_{nw}^* - S_{nwr}^*\right)^2 + \frac{4}{C}\left(S_{nw}^* - S_{nwr}^*\right)}\right) \tag{C.4}$$

where C is the Land's trapping coefficient defined as $C = \frac{1}{S_{nwr}^*} - \frac{1}{S_{nwi}^*} = \frac{1}{S_{nwrmax}^*} - 1$, S_{nwr}^* is the normalized residual non-wetting saturation expressed as $S_{nwr}^* = \frac{S_{nwr}}{1 - S_{w_i}}$, and S_{nwi}^* is the normalized initial non-wetting saturation expressed as $S_{nwi}^* = \frac{S_{nwi}}{1 - S_{w_i}}$ and .In this model, $S_{w_{irr}}$ is 0.2 and S_{nwrmax} is 0.4. $S_{w_{irr}}$ is the irreducible wetting phase saturation and S_{nwrmax} is the maximum residual non-wetting phase saturation. Based on the work from (Juanes et al., 2006), only the drainage relative permeability curve was used for the wetting phase.

Appendix D. Model parameters

The key fluid parameters influencing flow in the model can be found in Table D.1. Harvey's correlation for CO_2 Henry's constant was used, which makes the Henry's constant a function of pressure, temperature and salinity (Harvey, 1996). No dispersion or diffusion was included in this model.

Table D.1
Key fluid parameters influencing flow in the model.

Parameter	Values for 0° Dip	Values for 2° Dip
Water Density (Initial)	1008.5-1008.7 kg/m^3	1013.2-1001.4 kg/m3
Water Viscosity (Initial)	0.46 cp	0.46 cp
CO_2 Density (End of Injection)	664.1-669.8 kg/m3	594-664 kg/m3
CO_2 Viscosity	0.02-0.05 cp	0.047-0.054 cp
Vertical Temperature Gradient	—	—
Reservoir Temperature	65°C	65°C
Mass Fraction of Dissolved CO_2 at the End of Injection	0.102-0.119	0.102-0.118

Table D.2
Gravity number for varying permeabilities and dip angles of 0°, 1°, and 2° using the equation in (Nordbotten et al., 2005).

	10mD	50mD	100mD	500mD	1000mD
Dip= 0°	0.015	0.080	0.161	0.818	1.648
Dip= 1°	0.015	0.080	0.163	0.821	1.657
Dip= 2°	0.015	0.080	0.163	0.824	1.673

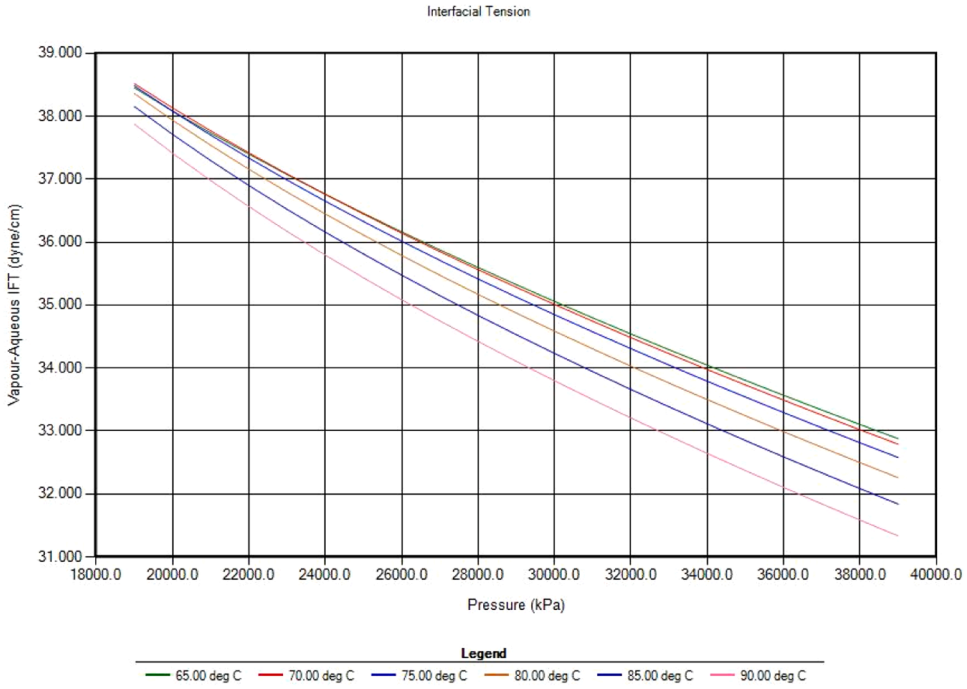

Fig. D.1. Interfacial Tension Curves from CMG WINPROP with a reservoir salinity of 30,000 mg/L.

The dimensionless gravity number was calculated using Equation D.1 below from the work of (Nordbotten et al., 2005):

$$N_g = \frac{\Delta\rho * g * k}{\mu_w \left(\frac{Q_t}{2\pi H^2}\right)} \tag{D.1}$$

The gravity number increases with increasing dip and for permeabilities greater than 100mD the gravity number increases with increasing reservoir dip angle. From (Nordbotten et al., 2005), N_g between 0.1 and 1, the gravity term becomes increasingly important.

The dimensionless capillary number was calculated using Equation D.2:

$$N_c = \frac{u * \mu_{CO_2}}{\sigma} \tag{D.2}$$

where σ is the interfacial tension (mN/m), $u = \frac{k * \Delta P}{\mu_{CO_2} * L}$ and μ_{CO_2} is the CO_2 viscosity. The interfacial tension was approximated using the CMG WINPROP at average reservoir pressure and temperature (Fig. D.1).

Table D.3
Capillary number by varying permeabilities and dip angles of 0°, 1°, and 2°.

	10mD	50mD	100mD	500mD	1000mD
Dip= 0°	1.5E-10	1.6E-10	1.7E-10	1.6E-10	1.3E-10
Dip= 1°	1.1E-10	3.8E-11	2.3E-10	1.9E-09	3.9E-09
Dip= 2°	6.2E-11	2.5E-10	6.6E-10	4.0E-09	8.2E-09

Appendix E. Areal footprint

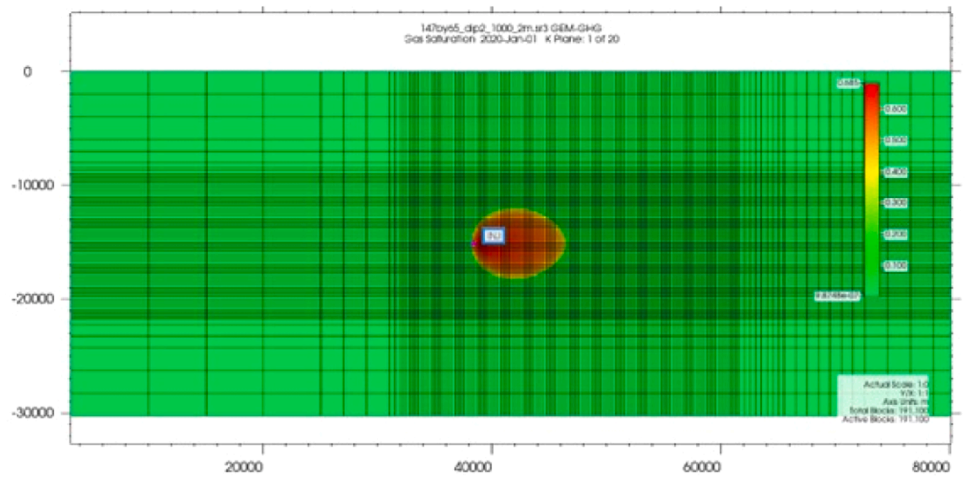

Fig. E.1. Areal footprint at the end of injection for 1000mD reservoir with 2° dip angle.

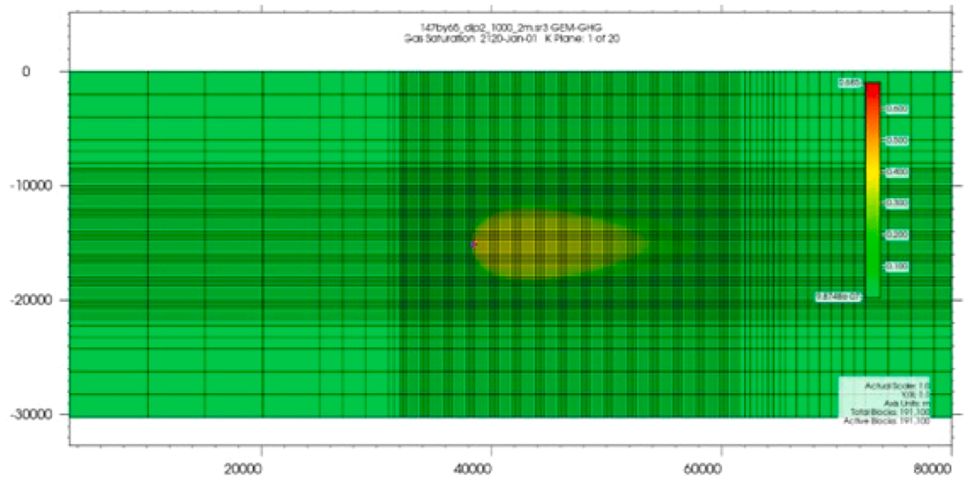

Fig. E.2. Areal footprint at 100 years post-injection for 1000mD reservoir with 2° dip angle.

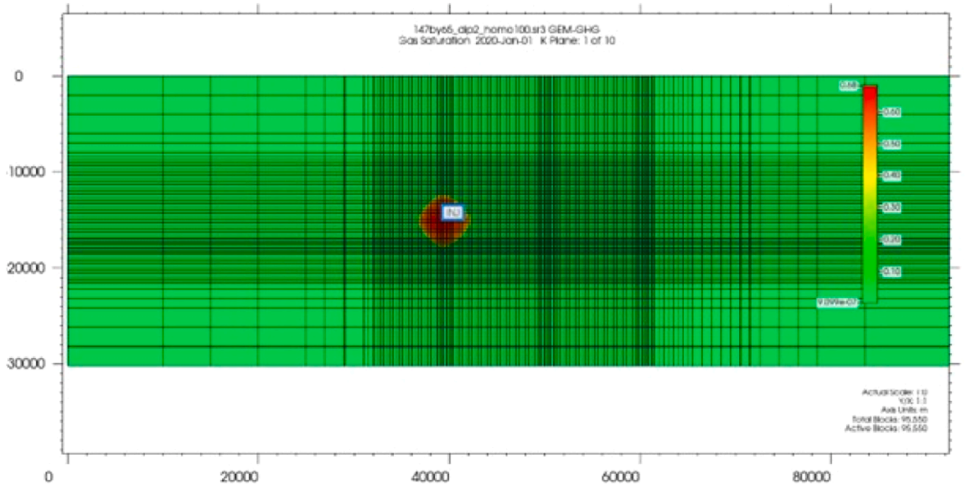

Fig. E.3. Areal footprint at the end of injection for 100 mD reservoir with 2° dip angle.

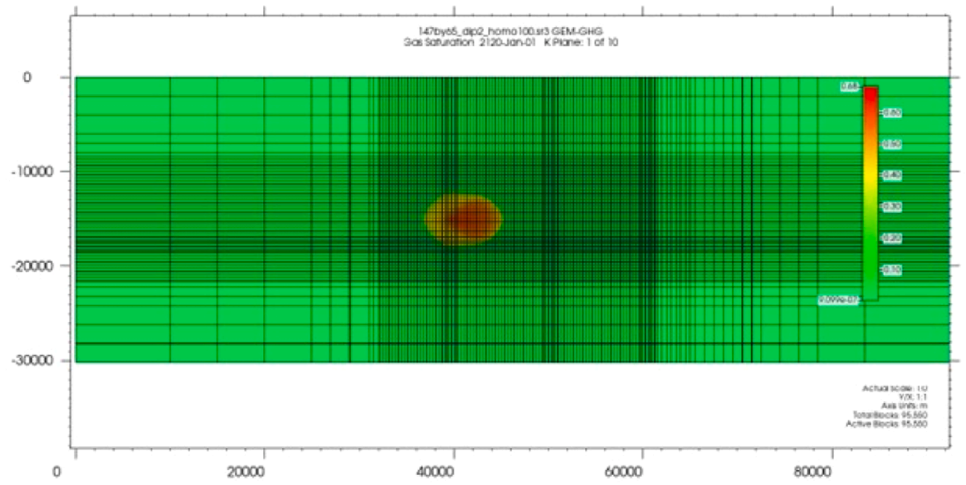

Fig. E.4. Areal footprint 100 years post-injection for 100 mD reservoir with 2° dip angle.

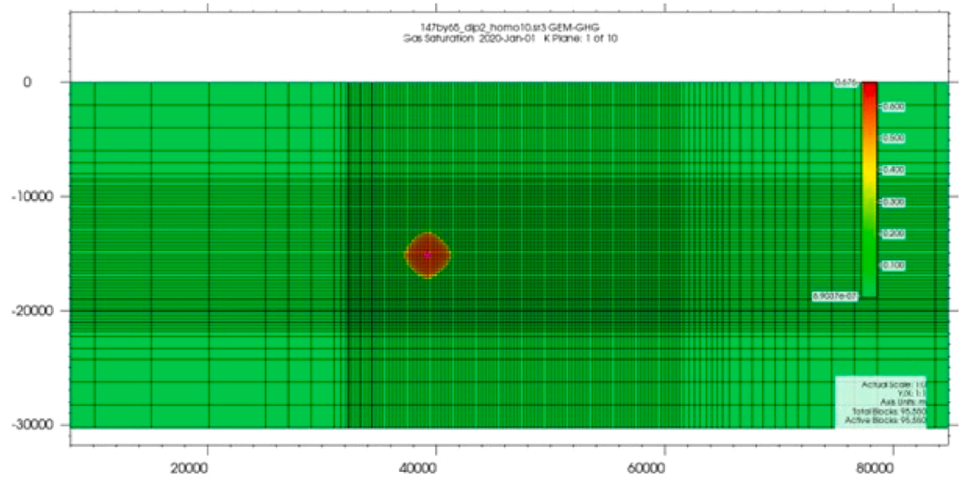

Fig. E.5. Areal footprint at the end of injection for 10 mD reservoir with 2° dip angle.

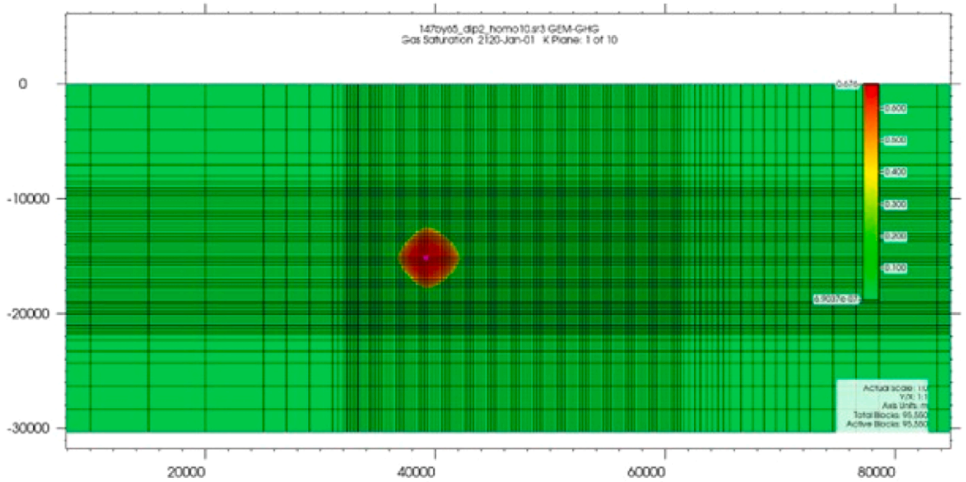

Fig. E.6. Areal footprint 100 years post-injection for 10 mD reservoir with 2° dip angle.

References

Brennan, S.T., 2014. The U. S. Geological Survey carbon dioxide storage efficiency value methodology: results and observations. Energy Procedia 63, 5123–5129. https://doi.org/10.1016/J.EGYPRO.2014.11.542.

Brooks, R.H., and Corey, A.T. (1964). Hydraulic Properties of Porous Media.

Callas, C., Davis, S.J., Saltzer, S.D., Hashemi, S.S., Wen, G., Gold, P.O., Zoback, M.D., Benson, S.M., and Kovscek, A.R. (2023). Criteria and workflow for selecting saline reservoirs for carbon storage. In [Manuscript in Preparation].

Callas, C., Saltzer, S.D., Davis, S.J., Hashemi, S.S., Kovscek, A.R., Okoroafor, E.R., Wen, G., Zoback, M.D., Benson, S.M., 2022. Criteria and workflow for selecting depleted hydrocarbon reservoirs for carbon storage. Appl. Energy 324, 119668. https://doi.org/10.1016/j.apenergy.2022.119668.

Chadwick, R.A., Arts, R., Bernstone, C., May, F., Thibeau, S., & Zweigel, P. (2008). Best practice for the storage of CO2 in saline aquifers: observations and guidelines from the SACS and CO2STORE projects. In British Geological Survey Occasional Publication No. 14. 10.1126/science.111.2891.578.

Chadwick, R.A., Zweigel, P., Gregersen, U., Kirby, G.A., Holloway, S., Johannessen, P.N., 2004. Geological reservoir characterization of a CO2 storage site: the Utsira Sand, Sleipner, northern North Sea. Energy 29 (9–10), 1371–1381. https://doi.org/10.1016/j.energy.2004.03.071.

Computer Modeling Group. (2019). CMG GEM Reference Manual 2019.10.

Doughty, C., 2010. Investigation of CO2 plume behavior for a large-scale pilot test of geologic carbon storage in a saline formation. Transp. Porous Media 82 (1), 49–76. https://doi.org/10.1007/S11242-009-9396-Z.

Doughty, C., Pruess, K., 2004. Modeling supercritical carbon dioxide injection in heterogeneous porous media. Vadose Zone J. 3 (3), 837–847. https://doi.org/10.2113/3.3.837.

Enick, R.M., Klara, S.M., 1990. Co2 solubility in water and brine under reservoir conditions. Chem. Eng. Commun. 90 (1), 23–33.

Frailey, S.M., 2013. Estimating CO2 plume size: a correlation for site screening. Int. J. Greenh. Gas Control 13, 230–234. https://doi.org/10.1016/j.ijggc.2012.11.033.

Gammer, D., Green, A., Holloway, S., Smith, G., 2011. The energy technologies institute's UK CO2 storage appraisal project (UKSAP). In: Society of Petroleum Engineers—Offshore Europe Oil and Gas Conference and Exhibition 2011, 2011. OE, pp. 1045–1058. https://doi.org/10.2118/148426-ms.

Goater, A.L., Bijeljic, B., Blunt, M.J., 2013. Dipping open aquifers—the effect of top-surface topography and heterogeneity on CO2 storage efficiency. Int. J. Greenh. Gas Control 17, 318–331. https://doi.org/10.1016/j.ijggc.2013.04.015.

Gupta, A.K., and Bryant, S.L. (2010). Analytical models to select an effective saline reservoir for CO2 storage. In SPE Annual Technical Conference and Exhibition (p. SPE-134762-MS). 10.2118/134762-MS.

Harvey, A.H., 1996. Semiempirical correlation for Henry's constants over large temperature ranges. AlChE J. 42, 1491–1494.

Hesse, M.A. (2008). Mathematical modeling and multiscale simulation of CO2 storage in saline aquifers. May, 1–208.

Hesse, M.A., Orr, F.M., Tchelepi, H.A., 2008. Gravity currents with residual trapping. J. Fluid Mech. 611, 35–60. https://doi.org/10.1017/S002211200800219X.

Hesse, M.A., Tchelepi, H.A., and Orr, F.M. (2006). Scaling analysis of the migration of CO2 in saline aquifers. Proceedings—SPE Annual Technical Conference and Exhibition, 5, 3001–3012. 10.2523/102796-ms.

IPCC. (2005). Global warming of 1.5°C. In IPCC Special Report on the impacts of global warming of 1.5°C above pre-industrial levels and related global greenhouse gas emission pathways, in the context of strengthening the global response to the threat of climate change.

Juanes, R., Macminn, C., Szulczewski, M., 2010. The footprint of the CO_2 plume during carbon dioxide storage in saline aquifers : storage efficiency for capillary trapping at the basin scale. Transp. Porous Media 82, 19–30. https://doi.org/10.1007/s11242-009-9420-3.

Juanes, R., MacMinn, C.W., 2008. Upscaling of capillary trapping under gravity override: application to CO2 sequestration in aquifers. In: SPE - DOE Improved Oil Recovery Symposium Proceedings, 2, pp. 1025–1040. https://doi.org/10.2118/113496-MS.

Juanes, R., Spiteri, E.J., Orr, F.M., Blunt, M.J., 2006. Impact of relative permeability hysteresis on geological CO2 storage. Water Resour. Res. 42 (12), 12418. https://doi.org/10.1029/2005WR004806.

Krevor, S., Blunt, M.J., Benson, S.M., Pentland, C.H., Reynolds, C., Al-Menhali, A., Niu, B., 2015. Capillary trapping for geologic carbon dioxide storage - From pore scale physics to field scale implications. Int. J. Greenh. Gas Control 40, 221–237. https://doi.org/10.1016/j.ijggc.2015.04.006.

Kumar, A., Noh, M., Pope, G.A., Sepehrnoori, K., Bryant, S., & Lake, L.W. (2004, September). Reservoir simulation of CO$_2$ storage in deep saline aquifers. SPE - DOE Improved Oil Recovery Symposium Proceedings. 10.2118/89343-ms.

Land, C.S., 1968. Calculation of imbibition relative permeability for two- and three-phase flow from rock properties. Soc. Pet. Eng. J. 8 (02), 149–156. https://doi.org/10.2118/1942-PA.

Litynski, J.T., Brown, B.M., Vikara, D.M., and Srivastava, R.D. (2011). Carbon capture and sequestration: the U.S. Department of Energy's R&D efforts to characterize opportunities for deep geologic storage of carbon dioxide in offshore resources. Offshore Technology Conference, Proceedings, 4(May), 3019–3028. 10.4043/21987-ms.

NETL. (2017a). Best Practices: Risk Management an Simulation for Geologic Storage Projects.

NETL. (2017b). Best Practices: Site Screening, Site Selection, and Site Characterization For Geologic Storage Projects.

Nordbotten, J.M., Celia, M.A., Bachu, S., 2005. Injection and storage of CO2 in deep saline aquifers: analytical solution for CO2 plume evolution during injection. Transp. Porous Media 58 (3), 339–360. https://doi.org/10.1007/s11242-004-0670-9.

Pini, R., Benson, S.M., 2017. Capillary pressure heterogeneity and hysteresis for the supercritical CO2/water system in a sandstone. Adv. Water Resour. 108, 277–292. https://doi.org/10.1016/j.advwatres.2017.08.011.

UNFCCC. (2017). Climate action now. Summary For Policymakers.

Van der Meer, L., 1995. The CO2 storage efficiency of aquifers. Energy Convers. Manag. 36 (6–9), 513–518.

Vella, D., Huppert, H.E., 2006. Gravity currents in a porous medium at an inclined plane. J. Fluid Mech. 555, 353–362. https://doi.org/10.1017/S0022112006009578.

Wang, F., Jing, J., Yang, Y., Liu, H., Sun, Z., Xu, T., Tian, H., 2017. Impacts of injection pressure of a dip-angle sloping strata reservoir with low porosity and permeability on CO2 injection amount. Greenh. Gases 7 (1), 92–105. https://doi.org/10.1002/GHG.1615.

Wen, G., Benson, S.M., 2019. CO2 plume migration and dissolution in layered reservoirs. Int. J. Greenh. Gas Control 87, 66–79. https://doi.org/10.1016/J.IJGGC.2019.05.012.

Wen, G., Hay, C., Benson, S.M., 2021. CCSNet: a deep learning modeling suite for CO2 storage. Adv. Water Resour. 155 https://doi.org/10.1016/j.advwatres.2021.104009.

Yamamoto, H., Doughty, C., 2011. Investigation of gridding effects for numerical simulations of CO2 geologic sequestration. Int. J. Greenh. Gas Control 5, 975–985. https://doi.org/10.1016/j.ijggc.2011.02.007.